Terahertz polarization conversion with quartz waveplate sets

Andrey K. Kaveev,[1,*] Grigory I. Kropotov,[1] Ekaterina V. Tsygankova,[1] Ivan A. Tzibizov,[1] Sergey D. Ganichev,[2] Sergey N. Danilov,[2] Peter Olbrich,[2] Christina Zoth,[2] Elizaveta G. Kaveeva,[3] Alexander I. Zhdanov,[4,7] Andrey A. Ivanov,[4] Ramil Z. Deyanov,[5] and Britta Redlich[6]

[1]TYDEX J. S. Co., 16 Domostroitelnaya str., St. Petersburg 194292, Russia

[2]Terahertz Center, University of Regensburg, Regensburg D-93040, Germany

[3]St. Petersburg State Polytechnic University, 26 Polytechnicheskaya str., St. Petersburg 194021, Russia

[4]Samara State Aerospace University, 34 Moskovskoye Schosse, Samara 443086, Russia

[5]Lomonosov Moscow State University, GSP-1 Leninskie gory, Moscow 119991, Russia

[6]FOM Institute Rijnhuizen, P.O. Box 1207, Nieuwegein NL-3430 BE, The Netherlands

[7]Current address: Samara State Technical University, 244 Molodogvardeyskaya str., Samara 443100, Russia

*Corresponding author: andreykaveev@tydex.ru

Received 12 September 2012; accepted 30 November 2012;
posted 11 December 2012 (Doc. ID 175976); published 21 January 2013

We present the results of calculation and experimental testing of an achromatic polarization converter and a composite terahertz waveplate (WP), which are represented by sets of plane-parallel birefringent plates with in-plane birefringence axis. The calculations took into account the effect of interference, which was especially prominent when plates were separated by an air gap. The possibility of development of a spectrum analyzer design based on a set of WPs is also discussed. © 2013 Optical Society of America

OCIS codes: 040.2235, 230.5440.

1. Introduction

The terahertz (THz) frequency range (300 GHz–10 THz) is quite a significant portion of the electromagnetic spectrum lying between microwave and infrared ranges. Unlike the latter, the THz range was virtually unexplored until recent times, due to the absence of powerful THz sources and detectors operating in this wavelength range. Promising applications of THz radiation include ultrafast secure data exchange, internal and external communications in integrated circuits, spectroscopy (namely, determining the chemical composition of complex substances, due to the fact that many vibrational and rotational levels of large organic molecules occur in the THz range), security and alarm systems, explosives, and weapon and drug detection [1–5]. Besides that, THz radiation can be very promising in tomographic and medical applications [4,6].

Development of femtosecond solid-state lasers and microelectronics during the last 15–20 years led to a breakthrough in THz research. Several new methods of signal generation were developed. THz radiation may be detected using various methods. The current state of scientific research and the existing technical background allow one to anticipate the development of commercially viable compact high-power sources and detectors of THz radiation [7–9].

1559-128X/13/040B60-10$15.00/0

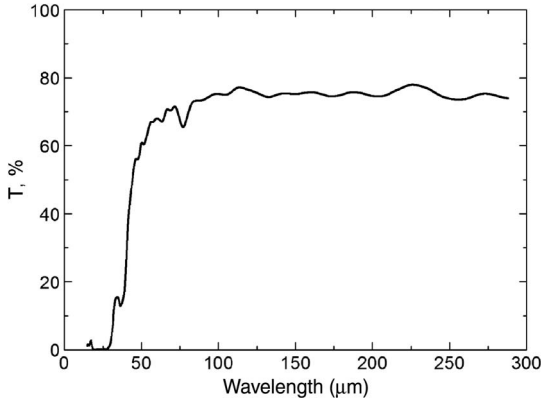

Fig. 1. Transmission spectrum of crystalline quartz, thickness 0.4 mm, x-oriented.

Rapid progress in THz optoelectronics necessitates the development of production of optical components for the THz spectral range as demanded by the specifics of the instruments operating in the aforementioned range. The material traditionally used for THz instrumentation is crystalline quartz. Its transmission spectrum in the spectral range of interest is shown in Fig. 1.

Besides that, crystalline quartz is a birefringent material [10]; this fact makes possible its use in THz optics to create polarization-converting components. In this paper, we present theoretical calculations and modeling as well as experimental studies of several such components based on crystalline quartz. It should be noted that instead of quartz, any other birefringent material transparent in the THz range may be used, such as sapphire or boron nitride. The birefringence axis must lie in the plane of the plates, which constitutes a technological limitation in the latter case.

2. Results

A. Achromatic Polarization Converters

In this work we have modeled, produced, and tested the wide wavelength-range THz polarization converter. In particular, it is a well-known achromatic waveplate (AWP) [11]. This object consists of a set of plane-parallel birefringent plates, which are transparent in the THz wavelength range with optical axes of birefringence lying in plane of the plate. Unlike monochromatic WP, which provides necessary phase retardation for a specific wavelength, AWP provides it in a wide wavelength range. By varying azimuth angles and plate thicknesses, one may achieve the achromatic effect in different wavelength ranges and also for different retardations (for example, $\lambda/4$ and $\lambda/2$).

1. Calculation

There are several papers [12–16] related to the calculation methods of quartz and sapphire AWPs. Some corrections were described in basic methods of WP calculations, because they are not suitable for the case when the measuring system has high resolution (as compared to the FWHM of interference peaks). So there were some modifications of methods that take into account the interference effect. In Tydex J. S. Co. we have applied the methods for real AWP calculations. Also, we have carried out the measurements of WP, produced on the basis of the simulations. These experiments confirm the applicability of the methods described. Thus the production of these objects is achieved.

According to Jones formalism [11,17] the system of several retardation plates is optically equal to system containing only two elements—the so called "retarder" and "rotator" (Fig. 2).

The retarder provides required phase shift (for example, π or $\pi/2$). The rotator turns the polarization plane at angle ω. There are two types of the polarization converter depending on the ω value: (1) ω is close to zero within the operating wavelength range. In this case, it is a common AWP, and its operating principle is the same as that of the monochromatic WP. For π—retardation, the polarization plane transmitted through AWP radiation is situated at 2θ to the polarizer axis, where θ is an angle of "effective optical axis" (EOA) of AWP. (2) ω depends on wavelength. In this case the object is not common "AWP" and may be called a broadband polarization converter (BBPC)—a special case of AWP. For example, in the case of circular-to-linear polarization transformation, the radiation transmitted through the converter has its polarization plane oriented at angle $\beta = \omega \pm 45°$ to the polarizer axis. In the case of linear-to-linear polarization transformation, $\beta = \omega + 2\theta$. In this work we have calculated AWPs and BBPCs for $\lambda/4$ and $\lambda/2$ cases in different THz ranges. Taking into account the interference effect, we have used [13] modified Jones matrix 4×4, written for each plate:

$$\hat{Q} = \begin{bmatrix} \cos k_e d & j n_e \sin k_e d & 0 & 0 \\ j\frac{1}{n_e} \sin k_e d & \cos k_e d & 0 & 0 \\ 0 & 0 & \cos k_0 d & j n_o \sin k_o d \\ 0 & 0 & j\frac{1}{n_o} \sin k_o d & \cos k_0 d \end{bmatrix}, \quad (1)$$

where $k_e = 2\pi n_e/\lambda$ and $k_o = 2\pi n_o/\lambda$, d is the thickness of the quartz plate, n_e and n_0 are respective refraction coefficients for extraordinary and ordinary

rays, and j is the imaginary unit. The resulting Jones matrix for the set of N plane-parallel plates is a product of N matrices given by Eq. (1) for each plate:

$$\hat{M} = \prod_{i=1}^{N} (\hat{F}_i \hat{Q}_i \hat{F}_i^{-1}), \tag{2}$$

where

$$\hat{F} = \begin{pmatrix} \cos\varphi & 0 & -\sin\varphi & 0 \\ 0 & \cos\varphi & 0 & -\sin\varphi \\ \sin\varphi & 0 & \cos\varphi & 0 \\ 0 & \sin\varphi & 0 & \cos\varphi \end{pmatrix} \tag{3}$$

is a 4×4 rotation matrix describing the angular orientation of the ith plate relative to the plane of polarization of incident radiation. The matrix $\hat{M}$ interrelates the electrical and magnetic field vectors of the incident, propagated, and reflected waves. The matrix that determinates the polarization of the incident wave given the (known) polarization of the propagated wave is as follows:

$$\hat{P} = \begin{pmatrix} \frac{M_{11}+M_{12}+M_{21}+M_{22}}{2} & \frac{M_{13}+M_{14}+M_{23}+M_{24}}{2} \\ \frac{M_{31}+M_{32}+M_{41}+M_{42}}{2} & \frac{M_{33}+M_{34}+M_{43}+M_{44}}{2} \end{pmatrix}. \tag{4}$$

To calculate the polarization of the propagated wave from the polarization of the incident wave, one may use the matrix $\hat{P}^{-1}$. That matrix is a kind of counterpart of the plain [11] 2×2 Jones matrix. Accounting for interference effect in the system of WPs shows that the system behaves differently when converting linear polarization to circular and vice versa.

The described system exhibits the properties of an AWP with fixed EOA alignment along polarizer axis x in the wavelength range where nondiagonal elements of a plain 2×2 Jones matrix

$$\hat{J} = \prod_{i=1}^{N} \hat{J}_i, \qquad \hat{J}_i = \begin{pmatrix} \cos\frac{\delta_i}{2} + j\cos(2\varphi_i)\sin\left(\frac{\delta_i}{2}\right) & j\sin(2\varphi_i)\sin\left(\frac{\delta_i}{2}\right) \\ j\sin(2\varphi_i)\sin\left(\frac{\delta_i}{2}\right) & \cos\frac{\delta_i}{2} - j\cos(2\varphi_i)\sin\left(\frac{\delta_i}{2}\right) \end{pmatrix}, \tag{5}$$

are near zero, modules of diagonal elements are about 1, and the phase difference between diagonal elements is equal to the specified retardation (here, $\delta_i = 2\pi(n_e - n_o)d_i/\lambda$, φ_i is the EOA angle of the plate relative to the polarizer axis).

Value set (δ_i, φ_i) corresponding to the ith WP can be calculated using the simulated annealing algorithm [15,18]. When calculating these values as noted above, depending on the minimization parameters, there are two possible cases: $\omega \approx$ const (for instance, 0), and $\omega \neq$ const. The ω value has a meaning of rotational angle of the "effective rotator."

Degree of polarization, i.e., the ratio of linearly polarized light intensity to total intensity, can be calculated as a function of wavelength. This degree is zero for completely circularly polarized light, whereas in the case of linear-to-circular polarization transformation (linear polarization along the x axis), the degree can be calculated as follows:

$$I = \frac{|E_2 \cdot \bar{E}_2 - E_1 \cdot \bar{E}_1|}{E_2 \cdot \bar{E}_2 + E_1 \cdot \bar{E}_1}, \tag{6}$$

where

$$\begin{aligned} E_1 &= P_{11}^{-1}\cos(\eta) + P_{21}^{-1}\sin(\eta), E_2 \\ &= P_{21}^{-1}\cos(\eta) - P_{11}^{-1}\sin(\eta), \eta \\ &= 0.5\arctan\left(\frac{P_{11}^{-1}\bar{P}_{21}^{-1} + P_{21}^{-1}\bar{P}_{11}^{-1}}{P_{11}^{-1}\bar{P}_{11}^{-1} - P_{21}^{-1}\bar{P}_{21}^{-1}}\right). \end{aligned} \tag{7}$$

Sample dependence for a BBPC is depicted in Fig. 3.

The EOA angle for a $\lambda/4$ polarization converter is related to the elements of the Jones matrix as follows:

$$\theta = 0.5\left|\operatorname{arctg}\left(\frac{\mathrm{Im}(P_{12}^{-1}e^{-j\nu})\mathrm{Re}(P_{11}^{-1}e^{-j\nu}) + \mathrm{Re}(P_{12}^{-1}e^{-j\nu})\mathrm{Im}(P_{11}^{-1}e^{-j\nu})}{\mathrm{Im}(P_{11}^{-1}e^{-j\nu})\mathrm{Re}(P_{11}^{-1}e^{-j\nu}) - \mathrm{Re}(P_{12}^{-1}e^{-j\nu})\mathrm{Im}(P_{12}^{-1}e^{-j\nu})}\right)\right|, \tag{8}$$

where $\nu_1 = 0.5\arg(-P_{12}^{-1}P_{21}^{-1})$, $\nu_2 = 0.5\arg(P_{11}^{-1}P_{22}^{-1})$—phase. The exponential factor in this equation is due to the fact that the counterpart plain Jones matrix $\hat{P}^{-1}$ is no longer described by Eq. (5). There are

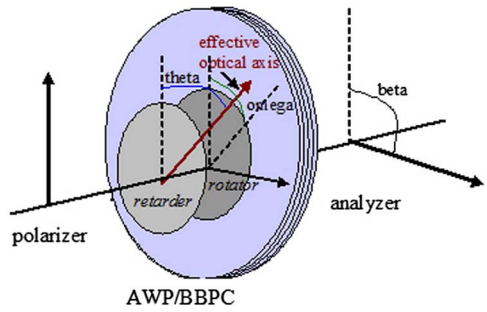

Fig. 2. (Color online) Schematic diagram of a set of plane-parallel birefringent media with in-plane birefringence axes.

two causes of this, namely, correction for interference and factoring in full phase incursion in the polarization converter. To use equations for δ, θ, and ω, which are valid for a plain Jones matrix (5), for approximate calculations, the matrix $\hat{P}^{-1}$ must be multiplied by $\exp(-j\nu)$. Phase values calculated with use of diagonal and nondiagonal matrix elements must be checked to verify that they are close to each other. Figure 4 depicts sample graph of phase ν versus the wavelength calculated for the same BBPC as shown in Fig. 3. In this case the graphs ν_1 for ν_2 are similar.

Angle ω may be calculated as follows:

$$\omega = \operatorname{arctg}\left(-\frac{\operatorname{Re}(P_{12}^{-1}e^{-j\nu})}{\operatorname{Re}(P_{11}^{-1}e^{-j\nu})}\right). \tag{9}$$

Finally, retardation of the system can be calculated as shown below. Given the matrix $\hat{P}^{-1}$ with near-zero nondiagonal elements,

$$\delta = \arg(P_{22}^{-1}) - \arg({}^{-1}P_{11}). \tag{10}$$

In general, the retardation can be calculated from a subset of $\hat{P}^{-1}$ matrix elements. For example,

$$\delta = 2\operatorname{arctg}\left(\left(\frac{(\operatorname{Im}(P_{11}^{-1}e^{-j\nu}))^2 + (\operatorname{Im}(P_{12}^{-1}e^{-j\nu}))^2}{(\operatorname{Re}(P_{11}^{-1}e^{-j\nu}))^2 + (\operatorname{Re}(P_{12}^{-1}e^{-j\nu}))^2}\right)^{0.5}\right). \tag{11}$$

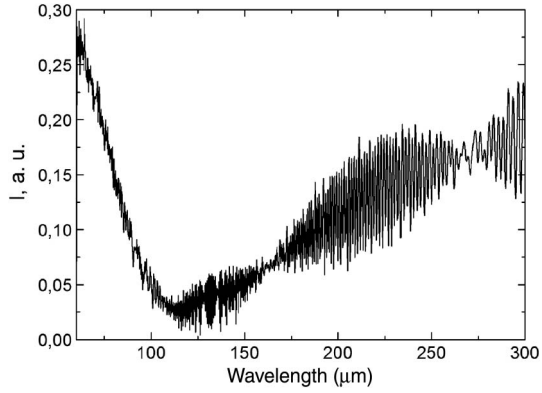

Fig. 3. Linearly polarized to total intensity ratio as a function of wavelength for the light converted to circular polarization using a BBPC designed for the 60–300 μm range.

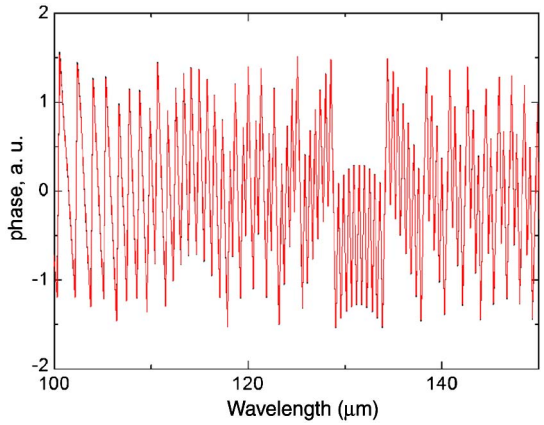

Fig. 4. (Color online) Phase versus wavelength for BBPC designed for 60–300 μm range.

Thus, a generic nonabsorbing achromatic polarization converter is described by three parameters, δ, θ, and ω. The latter must be taken into account, for example, when converting circular to linear polarization using a quarter-wave converter. Orientation of the polarization plane of the light output from the converter will depend on ω. The polarization plane of the light after the achromatic converter will be angled at $\omega \pm 45°$ relative to the polarizer axis.

Use of the matrix (1) instead of (5) is feasible when the interference must be taken into account due to practical considerations, for example, when the spectral bandwidth of the source is less than the typical width of the diffraction maximums. Wavelength bandwidth can be estimated from a simple formula, $\Delta\lambda = \lambda^2\Delta f/c$, where Δf is the frequency bandwidth. It should be compared to the interference period obtained from $\delta(\lambda)$ curve for the same wavelength. Whenever $\Delta\lambda$ exceeds interference period, the matrix (5) is generally sufficient for use.

Figure 5 depicts sample dependencies $\delta(\lambda)$, $\varphi(\lambda)$, and $\omega(\lambda)$ calculated for 2×2 and 4×4 Jones matrices (for the cases $\omega \approx$ const and $\omega \neq$ const) for a BBPC with two-sided antireflection coating. It can be seen that the general shapes of the curves for different Jones matrices are the same, but the interference effect, which is most prominent for $\varphi(\lambda)$ and $\delta(\lambda)$, leads to "noisiness" of the curves at specific wavelengths. The same effect is less eminent for $\omega(\lambda)$. It should be noted that the interference effect would be much more pronounced without antireflection coating. In the case of AWP, the $\delta(\lambda)$ and $\varphi(\lambda)$ curves will be similar, whereas the $\omega(\lambda)$ curve will be near constant, which can be seen, for example, in Fig. 5(d): throughout the entire range, the angle variation is less than 2°.

An important conclusion of the analysis described above is that two-sided antireflection coating is highly recommended for quarter-wave achromatic polarization converters to suppress the interference effect. The antireflection coating is accounted for in the analysis above by multiplying the expression (2) both on the left and on the right by matrix (1) describing such a coating.

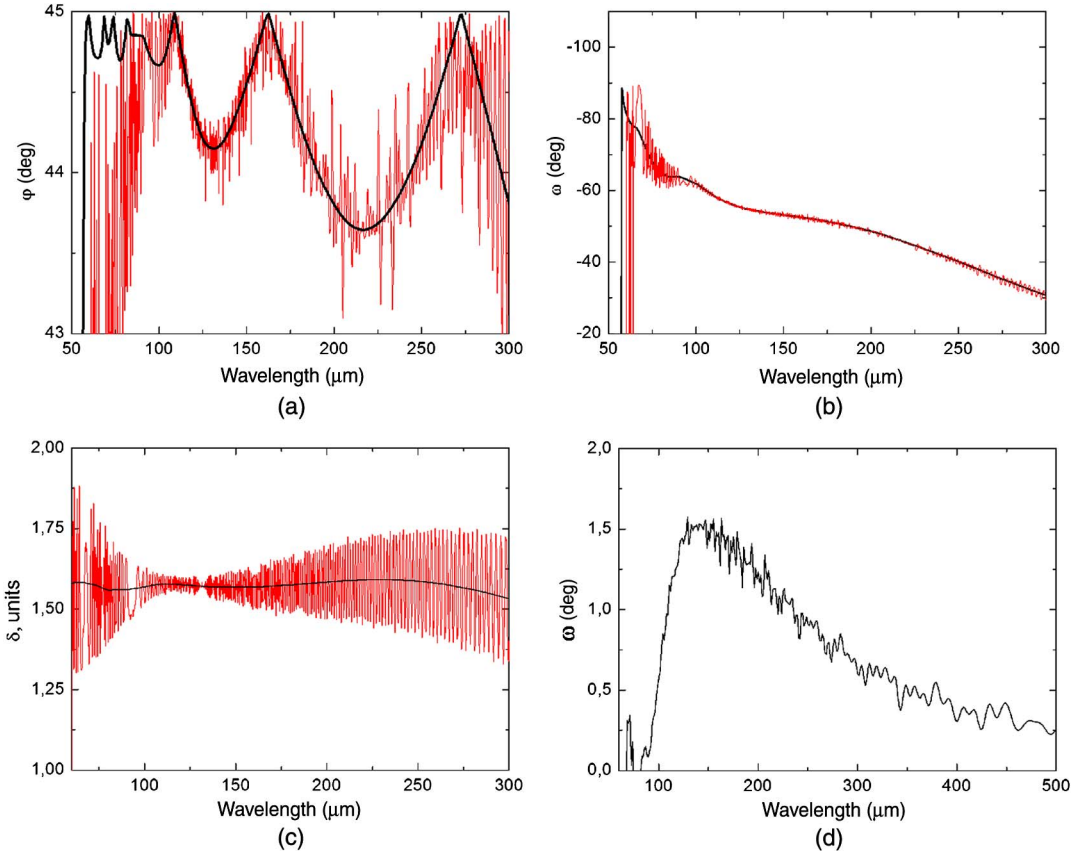

Fig. 5. (Color online) (a) EOA angle φ versus the wavelength in the cases of 2 × 2 (bold curve, no account for interference), and 4 × 4 (fine curve, with interference) Jones matrix. The calculation assumes BBPC ($\omega \neq$ const) designed for the 60–300 μm range. (b) "Effective rotator" rotation angle versus wavelength $\omega(\lambda)$ for the same BBPC. (c) Retardation versus wavelength $\delta(\lambda)$ for the same BBPC. (d) Sample of a dependence $\omega(\lambda)$ for an AWP designed for the same spectral range.

2. *Experimental Results*

Experimental approval of the method has been carried out with use of Fourier spectrometer Vertex 70. We have used quarter-wave BBPC for then 60–300 μm wavelength range. The results are shown in Fig. 6.

The figure depicts a set of transmission spectra of an AWP situated between two linear polarizers. Each spectrum in the set corresponds to a specific angular orientation of the analyzer. It can be seen that the variation of the transmittance values for each orientation is within the signal-to-noise ratio (SNR) of the Fourier spectrometer, which was in this case is about 1:100. This fact indicates that the transmittance of the system is not dependent on angular position of the analyzer, or, in other words, linear polarization of light is efficiently converted to circular in the specified spectral range 60–300 μm.

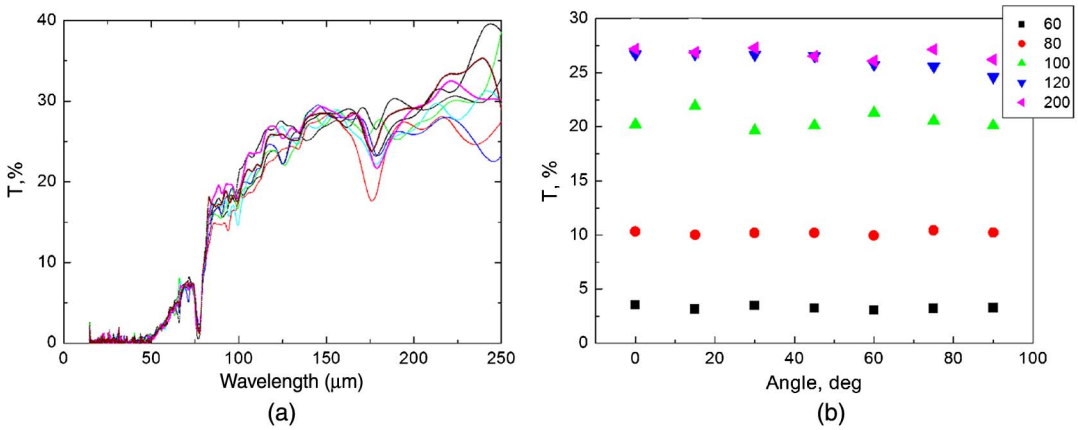

Fig. 6. (Color online) Dependence of linearly polarized light transmission for $\lambda/4$ BBPC on wavelength (a), same for different angles of analyzer [rotated linear polarizer, ordinate axis in (b)]. Each sequence in (b) corresponds to its own wavelength [upper right side of (b)] taken from (a). The curves in (a) are very similar. The small misfit of the curves is related to the relatively low SNR of the spectrometer.

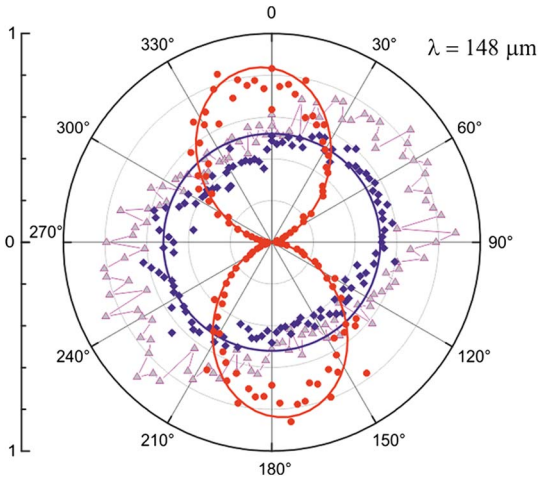

Fig. 7. (Color online) Laser radiation intensity versus analyzer rotation angle without AWP (circles) and with quarter-wave AWP (rhombi). Solid curves represent theoretical analyzer (eight-shape) and AWP (O-shape) characteristics. Triangles represent signal diagram for standard quarter-wave plate with rated wavelength 148 μm.

Optical properties of the discussed AWP were also studied using optically pumped THz molecular lasers: a high-power pulsed NH_3 laser operating at 90, 148, and 280 μm, as well as continuous-wave methanol laser operating at 118 μm [19–21]. Vertically polarized laser radiation passing through the quarter-wave AWP was measured as a function of the rotation angle of a linear analyzer downstream of the AWP. A quarter-wave plate situated at a specific angle between the direction of polarization of laser radiation and the optical axis transforms linear polarization to circular. Typical measured signal as a function of analyzer angle (rotated clockwise) is shown in Fig. 7. Circles represent the linear analyzer signal in the absence of AWP (wavelength 148 μm). The gray curve is an approximation of the analyzer signal by theoretical function $\cos^2\nu$, where ν is the analyzer rotation angle. Rhombi are the signal in the presence of AWP. It can be seen that AWP exhibits almost no deviation from perfect behavior. The same figure shows for comparison the signal diagram for a standard monochromatic quarter-wave plate (shown in triangles). The graph shows that, despite slightly higher light absorption, AWP generates better circular polarization. Some residual ellipticity (about 10%) may be ascribed to measurement error due to imperfect polarizer, etc.

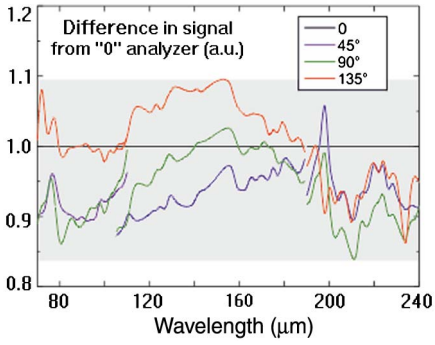

Fig. 8. (Color online) Spectral dependence of intensity of radiation generated by free-electron laser and passing though quarter-wave AWP at various analyzer angles.

Molecular lasers have a discrete generation spectrum with a fairly narrow generation line. AWP studies throughout the entire applicable wavelength range were carried out using a free-electron laser at FOM Institute Rijnhuizen, The Netherlands. [22,23] The experimental setup was similar. Figure 8 shows spectral dependencies of the signal at different analyzer angles. For illustrative purposes, the results are normalized to signal level at analyzer angle $\beta = 0$. It can be seen that relative signal deviation at various analyzer angles (including the effect of analyzer imperfection) is about ±10%. The measurements were carried out in increments of 15°, but for the sake of visualization, the results for intermediate β angles are not shown. They lie within the same bounds.

All experimental results are in agreement with the mathematical model used as a basis of design calculation of the achromatic polarization converter.

B. Composite Waveplates

Like achromatic polarization converters, composite waveplates (CWPs) are special assemblies of identical plates made of the same material. The paper [24] establishes that to achieve controlled adjustment of a retardation plate for a specific wavelength and arbitrary retardation, a set of three identical WPs is sufficient, with the outermost plates having parallel birefringence axes. Optical axes of the outermost plates are aligned, whereas the angle between them and the optical axis of the middle plate must be calculated using a certain method. After that, the assembly is set at a specific lateral angle to the electric field vector of the incident beam. This angle can be calculated by the same method as the angle between optical axes of the plates in the assembly. If the assembly allows one to adjust orientation angles (i.e., the plates are not in optical contact and not glued), the set may be fairly well adjusted for a series of arbitrary wavelengths and operate as a quarter-wave or half-wave plate. Rather than being achromatic or superachromatic, the composite retardation plates are controllable WPs.

1. *Calculation*

To evaluate CWP for specific retardation at a specific wavelength, one must first calculate [19] the rotation angle α of the middle plate using the equation

$$\alpha = 0.5 \arccos\left(\frac{\cos(\delta)\cos\left(\frac{\delta}{2}\right) - \cos\left(\frac{\delta_0}{2}\right)}{\sin(\delta)\sin\left(\frac{\delta}{2}\right)}\right), \qquad (12)$$

where $\delta = 2\pi n_o d/\lambda$, and δ_0 is the required retardation of the CWP. Reasonable plate thickness is selected to achieve CWP operation in the required wavelength range. The CWP's EOA rotation angle

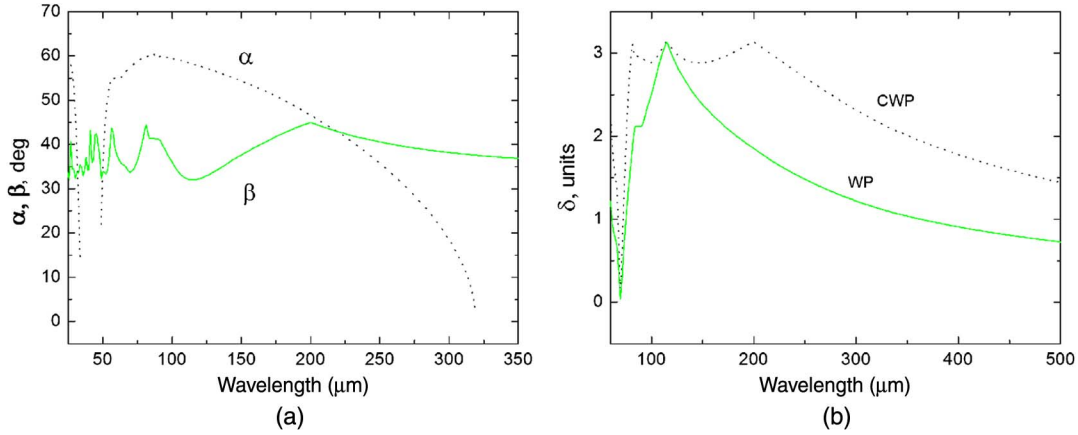

Fig. 9. (Color online) (a) Wavelength dependence of the middle plate rotation angle (α) and the assembly's EOA angle (β) calculated for CWP operating in the range of 60–300 μm. (b) Comparison of retardations of the said CWP and monochromatic WP rated for 118 μm.

β can be determined by substituting the calculated α value into Eq. (8) using matrix elements (5). Then the angles are corrected for interference. Figure 9(a) shows sample results of the calculation of these angles for a $\lambda/4$ CWP designed for operation in the 60–300 μm range, obtained using 2×2 Jones matrices (i.e., without correction for interference). Figure 9(b) compares retardation behavior of the aforementioned CWP at angles corresponding to $\lambda/4$ retardation at 118 μm with the same for monochromatic WP rated for 118 μm wavelength. It can be seen that at the indicated wavelength the CWP and common WP exhibit similar behavior.

Since the reconfigurable WP requires rotation of the middle plate relative to the outer ones, the design of the unit must provide an air gap between them. To evaluate such a system using Jones matrices, besides type (1) matrices one needs to introduce two matrices given by

$$\hat{Q}_0 = \begin{bmatrix} \cos 2\pi\frac{h}{\lambda_0} & j\sin 2\pi\frac{h}{\lambda_0} & 0 & 0 \\ j\sin 2\pi\frac{h}{\lambda_0} & \cos 2\pi\frac{h}{\lambda_0} & 0 & 0 \\ 0 & 0 & \cos 2\pi\frac{h}{\lambda_0} & j\sin 2\pi\frac{h}{\lambda_0} \\ 0 & 0 & j\sin 2\pi\frac{h}{\lambda_0} & \cos 2\pi\frac{h}{\lambda_0} \end{bmatrix}, \tag{13}$$

to describe the air gap. Here, h is the air-gap width, and λ_0 is the operational wavelength of the CWP. It should be noted that the air-gap requirement substantially increases the overall complexity of the unit's manufacture, because all the plates must be as parallel as possible, and the gap width must be kept at minimum (several micrometers). In the case of wedge-shaped gap the system may also be evaluated using the Jones method as long as the wedge's parameters are known, but it is unlikely in a practical situation. In such a case the calculation includes integration over small areas of the plates corresponding to actual gap width in each point.

For example, let us consider linear-to-circular transformation of polarization. Similar to the case of the achromatic converter, the wavelength dependence of the intensity ratio I of linearly polarized light to total intensity is given by Eq. (6). To find the minimum of this value by varying the angle pair (α, β) (i.e., respectively, the angular position of the middle plate relative to the outmost ones and overall unit rotation), one can use the following search algorithm. All parameters of Eq. (6) depend on these angles; therefore, a bivariate dependence $I(\alpha,\beta)$ can be constructed. Then the angle pair corresponding to the minimum I value can be found. Interference corrections to α and β introduced by substituting matrices (1) instead of (6) may amount to several angle degrees.

A prototype CWP is currently undergoing experimental validation. We do not report the results yet because the validation is not complete. But preliminary results are in agreement with the theory described above.

C. Concept of a Quartz Spectrum Analyzer

One more interesting application can be thought of for the systems of birefringent plates with birefringence axis lying in the plane of the plates. Namely, a set of three plates situated between two crossed polarizers can be used as a THz spectrum analyzer.

The general spectroscopic problem can be stated as follows [25]. Assume that a beam of light with unknown spectral content illuminates a system consisting of a nonselective (integral) radiation receiver and a spectroscopic attachment. The attachment can be described using generic instrument function $K(\lambda,\gamma)$, where λ is the wavelength of the incident radiation, and γ is a generalized coordinate describing control of the spectrometer. Some examples of such systems are the Fabry–Perot interferometer with instrument function [26] $K(\lambda,\gamma)\sim(1+\cos(2\pi\gamma/\lambda))$, the Michelson interferometer [27], etc. To solve the spectroscopic problem means to deduce the spectral distribution of the incident radiation from the response of the system with known instrument function. This

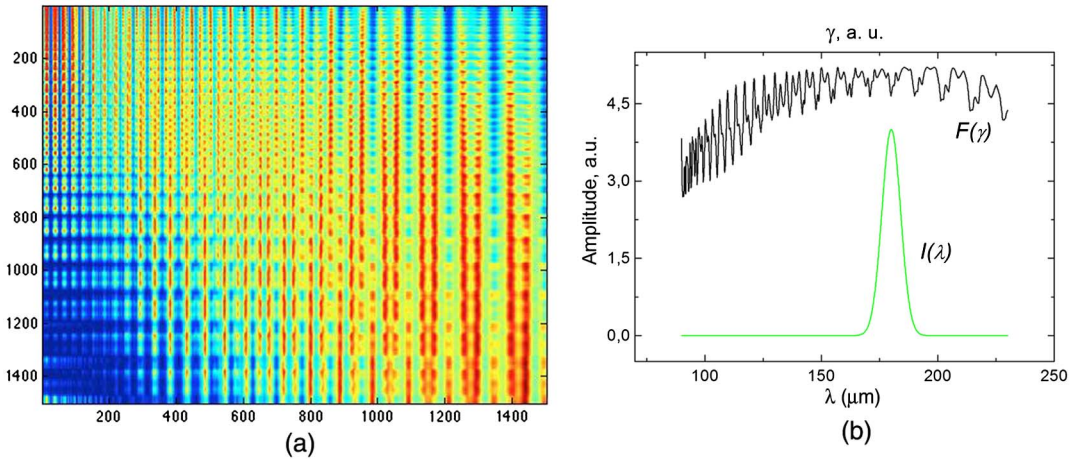

Fig. 10. (Color online) (a) Sample Fredholm kernel (horizontal and vertical axes correspond to λ and γ) and (b) sample response, i.e., $F(\gamma)$ for known Gaussian $I(\lambda)$.

problem is ill-conditioned and assumes solution of the Fredholm equation of the first kind,

$$\int_{\lambda 1}^{\lambda 2} K(\lambda,\gamma) I(\lambda) \mathrm{d}\lambda = F(\gamma). \tag{14}$$

Incident signal spectrum $I(\lambda)$ must be derived from the dependence $F(\gamma)$, which is measured experimentally by the instrument. Variation limits λ and γ are known. Fredholm kernel is the instrument function. Such problem can be solved by numerical methods, such as regularization, etc.

A set of quartz plates can be used as the "spectroscopic attachment." It was shown that to obtain the best solution of the problem, three plates are sufficient, with middle-to-outer plate thickness ratio about 0.8–1. Such conditions produce maximum rank of the matrix corresponding to the Fredholm kernel.

The analytical expression for the Fredholm kernel of such a system is very cumbersome. The kernel is the transmittance of a system of quartz plates between two crossed polarizers as a function of rotation angles of the plates. It is equal to the squared module of the nondiagonal element of the product of Jones matrices, which are, in the simplest case, given by Eq. (5). Interference corrections and accounts for the air gap required for plate rotation can be introduced using a method described in Section 2.B, i.e., by multiplying matrices (1) and (11). Sample kernel, $I(\lambda)$ and $F(\gamma)$, functions are shown in Fig. 10. In this case the parameter γ is a generalized coordinate describing the angular position of the middle plate relative to the outer plates, as well as angular position of the whole system. It can be seen that both the kernel and $F(\gamma)$ are very complex, whereas $I(\lambda)$ is quite simple.

Presently the authors are working on obtaining numerical solutions of this problem using known (model) functions $F(\gamma)$. Quantification of the equation leads to densely populated, ill-conditioned square matrices unstable in regard to right-side errors.

Thus, the solutions obtained using singular value decomposition and iterative methods (such as Seidel, Jacobi, Craig, and Lebedev) are against the physical meaning of the problem despite producing near-zero residuals $R\text{factor} = \|Ax - b\|/\|b\|$. One of the

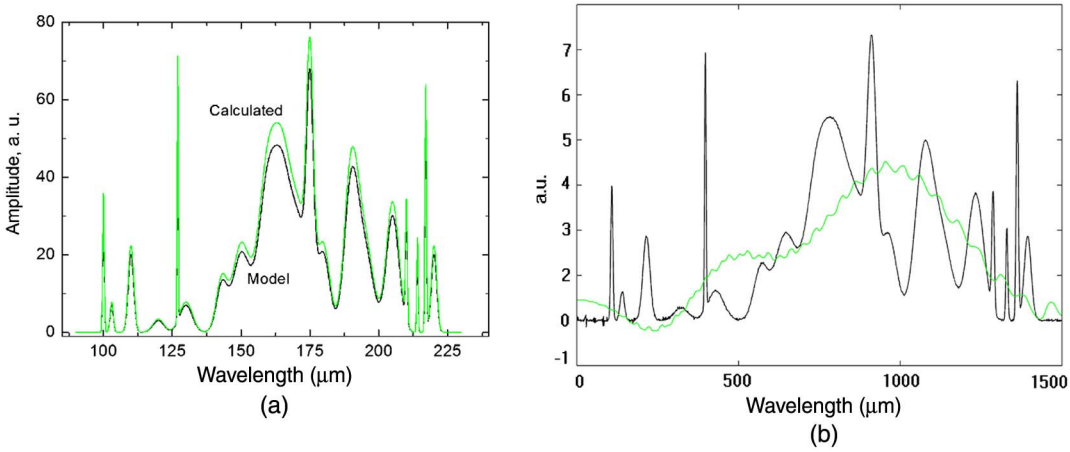

Fig. 11. (Color online) (a) Original and reconstructed $I(\lambda)$ represented by several overlapping peaks. Without right-side disturbance the function is reconstructed with adequate precision. (b) Solution obtained using Tikhonov regularization method at 1% disturbance of the right-side vector, and undisturbed solution.

possible methods to solve this problem is the global minimization approach [28] applied to the function $I(\lambda)$, which is represented by the superposition of symmetrical and asymmetrical peaks [see Fig. 11(a)]. Such an approach is physically meaningful in the context of spectrum analysis. Physically valid solutions were obtained by means of parameterization of asymmetric peaks using Edgeworth series [29]:

$$A(x) = A_G(x) + \sum_{k=3}^{\infty} (-1)^k \frac{\beta_k}{k!} A_G^{(k)}(x), \tag{15}$$

where $A_G, A_G^{(k)}$ are normal the density function and its derivatives, and β_k are quasi-momentums expressed through cumulants κ_n in a nonlinear way [29]. The Edgeworth series parameters were the coefficients $\gamma_n = \kappa_n/\kappa_2^{n/2}$, such as $\gamma_3 = \kappa_3/\kappa_2^{3/2}$ (peak asymmetry coefficient), and $\gamma_4 = \kappa_4/\kappa_2^2$ (excess coefficient that describes deviation of the distribution from normal to "pointer" or "flatter" vertex). Then we considered a finite Edgeworth series with cumulant coefficients $\gamma_1, \gamma_2, \ldots, \gamma_{10}$. Optimal values of the variates $\gamma_1, \gamma_2, \ldots, \gamma_{10}$ were obtained using the least-squares method:

$$F = \sum (Y_i^{\text{experim}} - Y_i^{\text{theor}})^2 \to \min. \tag{16}$$

The functional F was shown to be multiextremal, which led to crucial importance of the global functional minimization method [28].

However, the issue of solution instability in regard to disturbances of $F(\gamma)$ remains unsolved. This issue by all means can emerge in actual spectrum analysis experiment. The matrix of the problem is rank-deficient. It leads to substantial difficulties even when solving the problem without noise distortion of the right-side vector [see bold curve in Fig. 11(b)]. In the case when the source data are distorted by noise, one possible approach is the Tikhonov regularization method, which considers a problem of minimization of the following parametrical functional:

$$\Phi_\alpha(A, \tilde{b}, x) = \|Ax - \tilde{b}\|_2^2 + \alpha^2 \|Lx\|_2^2, \tag{17}$$

where α is the regularization parameter, $\tilde{b}$ is the representation of the right-side vector with random disturbances, x is the regularized solution of the problem, and L is the discrete first-order differential operator

$$L = \begin{pmatrix} 1 & -1 & 0 & \ldots & 0 & 0 \\ 0 & 1 & -1 & \ldots & 0 & 0 \\ \ldots & \ldots & \ldots & \ldots & \ldots & \ldots \\ 0 & 0 & 0 & \ldots & 1 & -1 \end{pmatrix}. \tag{18}$$

On the basis of [30], the authors have selected the parameter

$$\alpha^2 = \frac{\delta \times \sigma_{\max}^2(A)}{\|\tilde{b}\|_2 + \delta}, \tag{19}$$

assuming that the matrix A is precisely defined, and all disturbances are the disturbances of the right-side vector b, where $\|\tilde{b} - b\| \le \delta$, and $\sigma_{\max}(A)$ is the maximum singular value of the matrix A. The Tikhonov functional was minimized using extended regularized systems method [31].

The authors were able to deduce physically valid solutions, but their accuracy is still inadequate for practical purposes. The work on this problem continues. Figure 11(b) shows the regularized solution of the problem (fine curve) with 1% disturbance of the right side. Alternative methods were considered to select the regularization parameter, such as the L-curve method, the cross-validation method, and its generalization for stationary iterative methods. However, these attempts were unsuccessful. Development of a quartz spectrum analyzer continues.

3. Conclusions

We have demonstrated by experiments that sets of plane-parallel birefringent plates with in-plane birefringence axis are instrumental for THz polarization optics. We present results of calculations and experimental validation of an achromatic polarization converter and a CWP for THz spectral range, taking into account the interference effect and air gaps between the plates. A mathematical model is presented demonstrating the possibility of development of a spectrum analyzer design based on a set of WPs.

This work was supported by the Russian Foundation for Assistance to Small Innovative Enterprises (FASIE), Contract No. 9776r. The support by the DFG (SPP. 1459) is gratefully acknowledged. We also gratefully acknowledge the support by the Stichting voor Fundamenteel Onderzoek der Materie (FOM) in providing the required beam time on FELIX.

References

1. J. Federici, B. Schulkin, F. Huang, D. Gary, R. Barat, F. Oliveira, and D. Zimdars, "THz imaging and sensing for security applications—explosives, weapons and drugs," Semicond. Sci. Technol. **20**, S266–S280 (2005).
2. F. Friederich, W. von Spiegel, M. Bauer, F. Meng, M. Thomson, S. Boppel, A. Lisauskas, B. Hils, V. Krozer, A. Keil, T. Loffler, R. Henneberger, A. Huhn, G. Spickermann, P. Bolivar, and H. Roskos, "THz active imaging system with real-time capabilities," IEEE Trans. Terahertz Sci. Technol. **1**, 183–200 (2011).
3. K. Ajito and Y. Ueno, "THz chemical imaging for biological applications," IEEE Trans. Terahertz Sci. Technol. **1**, 293–300 (2011).
4. K. Humphreys, J. Loughran, W. Lanigan, T. Ward, J. Murphy, and C. O'Sullivan, "Medical applications of terahertz imaging: a review of current technology and potential applications in biomedical engineering," in *Proceedings of IEEE 26th Annual International Conference of the Engineering in Medicine and Biology Society* (IEEE, 2004), pp. 1302–1305.
5. X.-C. Zhang and J. Xu, *Introduction to THz Wave Photonics* (Springer, 2010).
6. Z. Taylor, R. Singh, D. Bennett, P. Tewari, N. Bajwa, M. Culjat, A. Stojadinovic, H. Lee, J.-P. Hubschman, E. Brown, and

W. Grundfest, "THz medical imaging: in vivo hydration sensing," IEEE Trans. Terahertz Sci. Technol. **1**, 201–219 (2011).
7. D. Stanze, A. Deninger, A. Roggenbuck, S. Schindler, M. Schlak, and B. Sartorius, "Compact cw terahertz spectrometer pumped at 1.5 μm wavelength," Int. J. Infrared Millim. Waves **32**, 225–232 (2011).
8. Z. Popovic and E. Grossman, "THz metrology and instrumentation," IEEE Trans. Terahertz Sci. Technol. **1**, 133–144 (2011).
9. F. Sizov and A. Rogalski, "THz detectors," Prog. Quantum Electron. **34**, 278–347 (2010).
10. F. Brehat and B. Wyncke, "Measurement of the optical constants of crystal quartz at 10 K and 300 K in the far infrared spectral range: 10–600 cm^{-1}," Int. J. Infrared Millim. Waves **18**, 1663–1679 (1997).
11. A. Yariv and P. Yeh, *Optical Waves in Crystals* (Mir, 1987).
12. J.-B. Masson and G. Gallot, "Terahertz achromatic quarter-wave plate," Opt. Lett. **31**, 265–267 (2006).
13. G. Savini, G. Pisano, and P. Ade, "Achromatic half-wave plate for submillimeter instruments in cosmic microwave background astronomy: modeling and simulation," Appl. Opt. **45**, 8907–8915 (2006).
14. S. Pancharatnam, "Achromatic combination of birefringent plates," Proc. Ind. Ac. Sci. **XLI**, 130–144 (1955).
15. J. Ma, J.-S. Wang, C. Denker, and H.-M. Wang, "Optical design of multilayer achromatic waveplate by simulated annealing algorithm," Chin. J. Astrophys. **8**, 349–361 (2008).
16. G. Kang, Q. Tan, X. Wang, and G. Jin, "Achromatic phase retarder applied to MWIR & LWIR dual-band," Opt. Express **18**, 1695–1703 (2010).
17. R. Jones, "A new calculus for the treatment of optical systems," J. Opt. Soc. Am. **31**, 488–503 (1941).
18. W. Press, W. Teukolsky, W. Vetterling, and B. Flannery, *Numerical Recipes in C. The Art of Scientific Computing* (Cambridge University, 1997).
19. P. Schneider, J. Kainz, S. D. Ganichev, V. V. Bel'kov, S. N. Danilov, M. M. Glazov, L. E. Golub, U. Roessler, W. Wegscheider, D. Weiss, D. Schuh, and W. Prettl, "Spin relaxation times of 2D holes from spin sensitive bleaching of inter-subband absorption," J. Appl. Phys. **96**, 420–433 (2004).
20. Z. D. Kvon, S. N. Danilov, N. N. Mikhailov, S. A. Dvoretsky, and S. D. Ganichev, "Cyclotron resonance photoconductivity of a two-dimensional electron gas in HgTe quantum wells," Phys. E **40**, 1885–1887 (2008).
21. S. D. Ganichev and W. Prettl, *Intense Terahertz Excitation of Semiconductors* (Oxford University, 2006).
22. D. Oepts, A. F. G. van der Meer, and P. W. van Amersfoort, "The free-electron-laser user facility FELIX," Infrared Phys. Technol. **36**, 297–308 (1995).
23. S. N. Danilov, B. Wittmann, P. Olbrich, W. Eder, W. Prettl, L. E. Golub, E. V. Beregulin, Z. D. Kvon, N. N. Mikhailov, S. A. Dvoretsky, V. A. Shalygin, N. Q. Vinh, A. F. G. van der Meer, B. Murdin, and S. D. Ganichev, "Fast detector of the ellipticity of infrared and terahertz radiation based on HgTe quantum well structures," J. Appl. Phys. **105**, 013106 (2009).
24. M. Darsht, "The effect of an environment and external impacts on the polarized light propagation," Ph.D. thesis (Chelyabinsk State Technical University, 1996, in Russian).
25. A. Tichonov, *Methods of Incorrect Problems Solving* (Nauka, 1979).
26. A. Zhiglinsky and V. Kuchinsky, *Real Fabry–Perot Interferometer* (Mashinostroyeniete, 1983).
27. http://plasma.karelia.ru/~ekostq/PUBLIC/fs/index_2.html.
28. R. Deyanov and B. Schedrin, "Algorithm of subsequent descent on local minima system," Appl. Math. Inf. **30**, 46–54 (2008).
29. A. Malakhov, *Cumulant Analysis of Random Non-Gaussian Processes and their Transformations* (Sovetskoye Radio, 1978, in Russian).
30. A. Tikhonov and V. Arsenin, *Solution Methods for Ill-Conditioned Problems* (Nauka, 1986, in Russian).
31. A. I. Zhdanov, "The method of augmented regularized normal equations," Comput. Math. Math. Phys. **52**, 194–197 (2012).